arXiv:1608.03443v1 [physics.atom-ph] 11 Aug 2016

Optical vortices discern attosecond time delay in electron emission from magnetic sublevels

J. Wätzel and J. Berakdar
Institute for Physics, Martin-Luther-University Halle-Wittenberg, 06099 Halle, Germany
(Dated: October 2, 2016)

Photoionization from energetically distinct electronic states may have a relative time delay of tens of attoseconds. Here we demonstrate that pulses of optical vortices allow measuring such attoseconds delays from magnetic sublevels, even from a spherically symmetric target. The difference in the time delay is substantial and exhibits a strong angular dependence. Furthermore, we find an atomic scale variation in the time delays depending on the target orbital position in the laser spot. The findings offer thus a qualitatively new way for a spatio-temporal sensing of the magnetic states from which the photoelectrons originate, with a spatial resolution way below the diffraction limit of the vortex beam. Our conclusions follow from analytical considerations based on symmetry, complemented and confirmed with full numerical simulations of the quantum dynamics.

I. INTRODUCTION

The development of attosecond (*as*) optical sources is a major achievement. Beside technological applications, attosecond spectroscopy and metrology shed light on new and old fundamental problems that were hitherto experimentally inaccessible (cf. [1]). An illuminating example is the recent revival of the issues of time and time delay in tunneling and photoionization [2–7] which dates back to early applications of quantum mechanics to study the variation of the scattering-amplitude phase with the wave vector during collision processes [8–10]. Combining *as* XUV pulses and infrared (IR) streaking fields, the relative time delay of photo emitted electrons from different atomic levels was reported [11] (for an overview, see e.g. [2, 12, 13]). The finding triggered theoretical activities with a varying level of success in reproducing the experiments [14–25] but pointing out the role of electronic correlations, the directional dependence of the emitted electrons, laser fields effects, as well as the influence of resonances and Cooper minima.

Here we draw attention to another aspect of time-resolved photoelectron chronoscopy when utilizing spatially phase-structured (singular) laser fields, i.e. optical vortices [26–33]. Such beams can transfer orbital angular momentum (OAM) when interacting with matter [34–40] and have found numerous applications in a number of fields in science [41–53]. The OAM phase front forms a helical shape characterized by $\exp(im_{\mathrm{OAM}}\varphi)$, where φ is the azimuthal angle with respect to the propagation direction, and m_{OAM} is an integer winding number called the topological charge. OAM carrying laser beams are routinely realized, e.g. as Laguerre-Gaussian (LG) modes. Each photon may transfer a quantized OAM of $m_{\mathrm{OAM}}\hbar$. Beams with more than $m_{\mathrm{OAM}}\hbar = 300$ were demonstrated offering the opportunity to access excitations way beyond the limit set by the conventional optical propensity rules [54, 55] (degeneracy of involved states is also important [56]). Hence, vortices offer a new optical key to access magnetic sublevels [56] which is the starting idea of this work.

We consider an XUV, OAM carrying LG beam ionizing an initially completely symmetric target such as Ar atoms or C_{60} molecules. For the experimental feasibility and trapping properties of LG beams we refer to [57] and others [58–63]. As the amount of transferred OAM depends strongly on the orbital location in the laser spot [55, 56, 64–66], and the predicted time delay is explicitly related to the transferred OAM we predict a spatial resolution on orbitals having time-delay.

A. Background

The quantity of interest is the dependence of the time delay τ in photoionization on the light topological charge. Usually, in the experiment τ receives two contributions τ_{W} and τ_{CLC}. The Wigner time delay τ_{W} is related to the photoionization process triggered by the XUV pulse. The Coulomb-laser coupling term τ_{CLC} is akin to photoelectron motion in the combined Coulomb-streaking field, and hence is a setup-dependent quantity [20, 67]. We concentrate here on Wigner time delay as a system-sensitive quantity [93]. The time delay of a specific subshell is the average contributions over all magnetic sub-states, labelled m_i. For linearly polarized light the photoionization probabilities of states with $\pm m_i$ are equal and so are their contributions to the time delay. Also the angular dependence of photoelectrons emitted from these states are identical. Irradiation with OAM beams allows for transitions involving a change in magnetic quantum numbers by a maximal amount set by m_{OAM}. We will show explicitly for Ar atom and a fullerene cluster that a short XUV-OAM pulse ([69–71]) ionizes preferentially specific magnetic sublevels. Consequently, in certain directions the photoionization (and hence the time delay) is dominated by a specific magnetic sublevel, depending on the atom position in the beam. The time delay may serve so as a tool to identify the origin of the photoelectron in energy, magnetic state, and space.

II. MODEL

In a gauge where the scalar potential vanishes the interaction hamiltonian reads (atomic units are used) $\hat{H}_{\mathrm{Int}} = \hat{\boldsymbol{p}} \cdot \boldsymbol{A}(\boldsymbol{r}, t) + \boldsymbol{A}(\boldsymbol{r}, t) \cdot \hat{\boldsymbol{p}}$, where $\hat{\boldsymbol{p}}$ is the momentum operator and $\boldsymbol{A}$ is the vector potential with polarization vector $\hat{\epsilon} = (1, i)$, waist w_0, temporal envelope $g(t) = \cos[\pi t/nT]^2$, where $T = 2\pi/\omega$ is the cycle duration and n is the number of optical cycles. The explicit form of $\boldsymbol{A}$ is given in

appendix A. We focus on Ar target atom. Technicalities for C_{60} are in appendix F. For Ar the involved initial states are captured by the effective single-particle potential [72] $V(r) = -(1 + 5.4e^{-r} + 11.6e^{-3.682r})/r$, which proved useful for similar problems [73]. $V(r)$ misses correlation effects [74], yet the energetic position of the Cooper minimum is reasonably well reproduced [24]. Note, we consider photoemitted electrons and do not study the hole dynamics upon electron removal [75, 76]. From symmetry considerations when applying OAM beams a hole current is expected to emerge which orbitally magnetizes the residual ion. Obviously $|\mathbf{A}|^2$ has a donut shape (appendix A). An Ar atom in the donut center experiences only a weak intensity justifying so a non-relativistic perturbative treatment even for moderately intense fields (the frequency is in the XUV). As the atoms might be distributed over the beam, some would experience the peak intensity. However, as shown below these atoms show no reaction to a topological charge change and hence no time delay (because the transferrable angular momentum refers to the optical axis not the atom center). Hence the two types of atoms, located in the donut center or on its ring, should be distinguishable by measuring the time delay. Here, the electric field starts with a zero amplitude at the vortex center reaching, at a distance of 10 a.u., a peak amplitude of 1 a.u. [93]. It is important to remark that the time delay dependence on m_{OAM} diminishes rapidly as the atom is displaced (say by 2 a.u.) from the vortex center so that the high intensity region is irrelevant for the time delay discussed here. We note (and explicitly demonstrate below) that due to the laser donut-type intensity profile, orbitals with larger extension such as for fullerenes show similar effect as for atoms, but at intensity orders of magnitudes smaller than needed for atoms (this difference between Ar and C_{60} is two orders of magnitude). As the effect is of a general nature, we expect the proposed scheme to be useful also for extended systems.

Concerning the emitted electron, its wave function is expressible in a standard way [77] as $\Phi(\boldsymbol{r}, t) = \int \mathrm{d}\boldsymbol{k}\, a(\boldsymbol{k}, t)\varphi_{\boldsymbol{k}}^{(-)}(\boldsymbol{r})e^{-i\varepsilon_k t}$. The projection coefficients $a(\boldsymbol{k}, t)$ determine the photoionization amplitude as follows: The photoinduced emission of an electron initially in the bound state labeled $|\Psi_i(\boldsymbol{r})\rangle$ with energy ε_i to the continuum state $\varphi_{\boldsymbol{k}}^{(-)}(\boldsymbol{r})$ with the wave vector $\boldsymbol{k}$ and energy $\varepsilon_{\boldsymbol{k}} = k^2/2$ reads [77]

$$a_i(\boldsymbol{k}) = -i \int_{-\infty}^{\infty} \mathrm{d}t' \langle \varphi_{\boldsymbol{k}}^{(-)} | \hat{H}_{int}(t) | \Psi_i \rangle e^{i(\varepsilon_{\boldsymbol{k}} - \varepsilon_i)t}. \tag{1}$$

As established [20, 77–79] we expand in spherical harmonics $Y_{\ell m}(\Omega)$ as $\Psi_i(\boldsymbol{r}) = R_{n_i\ell_i}(r)Y_{\ell_i m_i}(\Omega_{\boldsymbol{r}})$ and $\varphi_{\boldsymbol{k}}^{-}(\boldsymbol{r}) = \sum_{\ell=0}^{\infty}\sum_{m=-\ell}^{\ell} i^{\ell} R_{k\ell}(r)e^{-i\delta_\ell(k)}Y_{\ell m}^{*}(\Omega_{\boldsymbol{k}})Y_{\ell m}(\Omega_{\boldsymbol{r}})$. The radial wave functions $R_{k\ell}$ are normalized as $\langle R_{k\ell}|R_{k'\ell}\rangle = \delta(\varepsilon_k - \varepsilon_{k'})$. The scattering phases are given by $\delta_\ell(k) = \sigma_\ell(k) + \eta_\ell(k)$ where $\sigma_\ell(k) = \arg[\Gamma(\ell + 1 - i/k)]$ is the Coulomb phase shift [10]. The quantity $\eta_\ell(k)$ is due to short range phase interactions [20].

For an analytical model let us consider *as* OAM pulse with $\hat{\epsilon} = (1, i)^T$, $m_{\mathrm{OAM}} = 1$, and the atom is in the donut center. We find $\nabla \cdot \boldsymbol{A}(\boldsymbol{r}, t) = 0$ and $e^{-\rho^2/w_0^2} = 1$ for $w_0 = 50\,\mathrm{nm}$. The angular ($\Omega_{\boldsymbol{k}} = (\vartheta_k, \varphi_k)$) dependent projection coefficients (1) and the reduced radial matrix elements $d^{m_{\mathrm{OAM}}}_{\ell,n_i\ell_i}$ are given in appendix B. The photoionization probability $w_i(\varepsilon_k, \Omega_{\boldsymbol{k}}) = |a_i(\boldsymbol{k})|^2$ is peaked around the center of energy (COE) given as $\varepsilon_{\mathrm{COE}} = \omega + \varepsilon_i$ and $k_{\mathrm{COE}} = \sqrt{2\varepsilon_{\mathrm{COE}}}$.

III. RESULTS AND INTERPRETATIONS

The photoionization amplitudes from the magnetic sublevels m_i of the $3p$ subshell have the structure

$$a_i(k_{\mathrm{COE}}, \Omega_{\boldsymbol{k}}) = \begin{cases} S_{m_{\mathrm{OAM}}+2, m_{\mathrm{OAM}}} Y_{m_{\mathrm{OAM}}+2, m_{\mathrm{OAM}}}(\Omega_{\boldsymbol{k}}) + \\ S_{m_{\mathrm{OAM}}+2, m_{\mathrm{OAM}}} Y_{m_{\mathrm{OAM}}, m_{\mathrm{OAM}}}(\Omega_{\boldsymbol{k}}) & m_i = -1, \\ S_{m_{\mathrm{OAM}}+2, m_{\mathrm{OAM}}+1} Y_{m_{\mathrm{OAM}}+2, m_{\mathrm{OAM}}+1}(\Omega_{\boldsymbol{k}}) & m_i = 0, \\ S_{m_{\mathrm{OAM}}+2, m_{\mathrm{OAM}}+2} Y_{m_{\mathrm{OAM}}+2, m_{\mathrm{OAM}}+2}(\Omega_{\boldsymbol{k}}) & m_i = 1, \end{cases}$$

$$S_{\ell,m} = \mathcal{E}_{-}(\varepsilon_{\mathrm{COE}}) d^{m_{\mathrm{OAM}}}_{\ell,n_i\ell_i} i^{-\ell} e^{i\delta_\ell(k_{\mathrm{COE}})} \begin{pmatrix} \ell & m_{\mathrm{OAM}}+1 & 1 \\ -m & m_{\mathrm{OAM}}+1 & m_i \end{pmatrix} \tag{2}$$

(cf. appendix A for $\mathcal{E}_{-}(\varepsilon_{\mathrm{COE}})$). These relations impose the propensity rules $\ell - \ell_i = \Delta\ell \leq m_{\mathrm{OAM}} + 1$ for $\ell_i + \ell + m_{\mathrm{OAM}}$ is odd, and $m - m_i = \Delta m = m_{\mathrm{OAM}} + 1$. Photoelectrons originating from $m_i = 0$ avoid the $x - y$ plane (i.e. $\vartheta_{\boldsymbol{k}} = \pi/2$) since the spherical harmonics $Y_{\lambda,\lambda-1}(\Omega_{\boldsymbol{k}})$ have a node at $\vartheta_{\boldsymbol{k}} = \pi/2$. The emission probability $|a_i(\boldsymbol{k})|^2$ exhibits no angular dependence in the equatorial plane. Around the Cooper minimum transitions to lower orbital angular momenta are weaker [80]. The energetic position of the minimum depends strongly on the angular momentum of the perturbative field. Fig. 1(a) shows the radial matrix elements for $m_{\mathrm{OAM}} = 1$. The relevant transitions according to the scheme (2) are the transitions $\ell_i = 1 \to \ell = 3$ and $\ell_i = 1 \to \ell = 1$. Around a laser frequency of $\omega = 95\,\mathrm{eV}$ we find that the expectedly dominant $d^{m_{\mathrm{OAM}}=1}_{\ell=3,\ell_i=1}$ has a comparable magnitude as $d^{m_{\mathrm{OAM}}=1}_{\ell=1,\ell_i=1}$. A strong angular dependence of the time delay is expected in the energy regime where the strengths of both ionization channels are comparable, for the interference between both channels delivers eventually the angular modulation [25]. This motivates our choice of the frequency regime, both for Ar and C_{60}. The underlying physics of time delay both for Ar and C_{60} is similar, and we will elaborate here on Ar deferring C_{60} case to appendix F. For $\omega = 100\,\mathrm{eV}$ the Ar photoionization probability dependence on the photoelectron emission angle $\vartheta_{\boldsymbol{k}}$ is shown in Fig. 2 for different initial states m_i. For a topological charge $m_{\mathrm{OAM}} = 1$ and $m_i = 1$, the ionized electron ends up in the f-partial wave channel with $m = 3$, while the counter-rotating photoelectron ends up in a superposition of the p and f partial wave channels with $m = 1$. A photoelectron lauched from $m_i = 0$ is described by the f partial wave channel with $m = 2$, i.e. the node of the spherical harmonic $Y_{3,2}(\vartheta_k = \pi/2, \varphi_k)$ leads to vanishing emission in this direction. In the $x - y$ plane ($\vartheta_{\boldsymbol{k}} = \pi/2$) the co-rotating electron with $m_i = 1$ relative to the circularly polarized OAM-field is dominant over the counter-rotating one with $m_i = -1$. The electron with $m_i = 0$

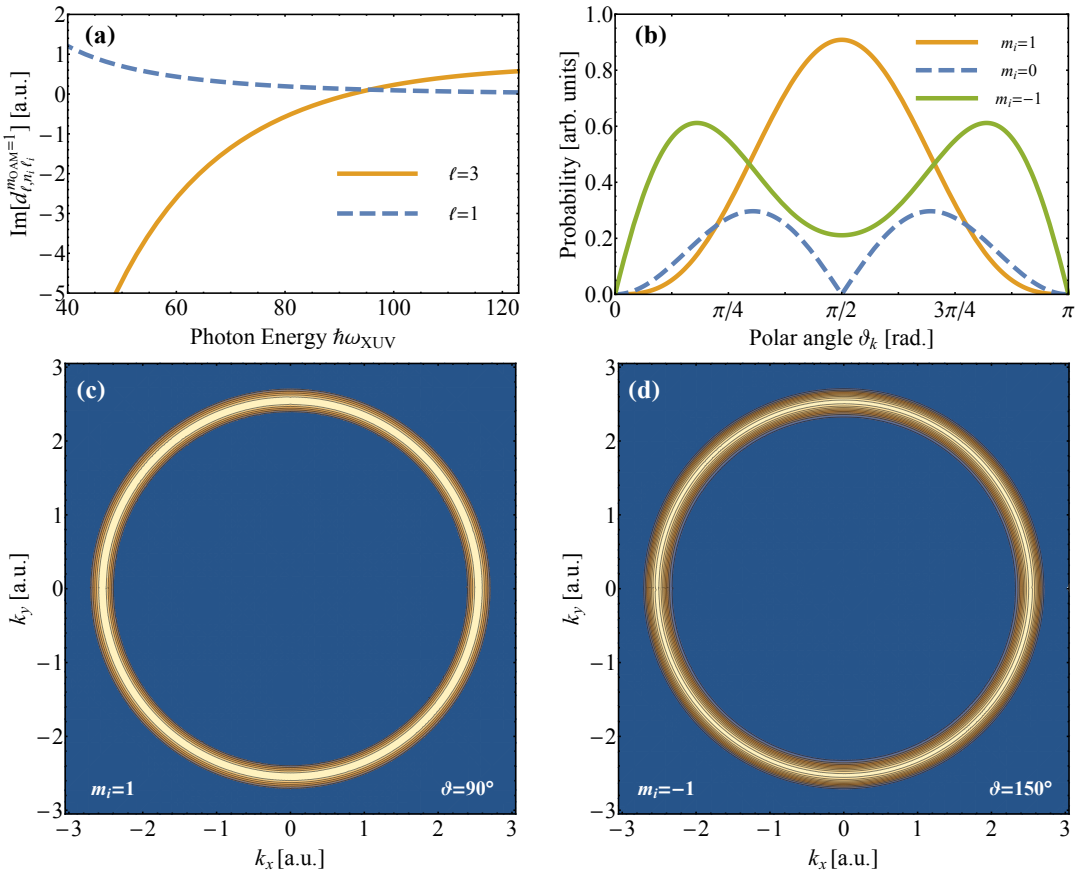

FIG. 1. (a) Reduced radial matrix elements for partial wave functions with orbital angular momenta $\ell = 3$ and $\ell = 1$. (b) Photoionization probabilities for the three different initial states of $3p$ subshell in argon. (c) and (d) photoelectron momentum distribution corresponding to $m_i = 1$ at $\vartheta_{\boldsymbol{k}} = 90°$ and $m_i = -1$ at $\vartheta_{\boldsymbol{k}} = 150°$. The beam has waist $w_0 = 50\,\mathrm{nm}$ and is $n = 10$ optical cycles long.

does not escape in this direction. Interestingly, the two types of electrons are predominantly emitted in different directions (at $\vartheta_{\boldsymbol{k}} = 150°$ the counter-rotating electron dominates the co-rotating one) allowing thus a discrimination via angular resolved photoelectron detection.

IV. ATTOSECOND TIME DELAY

The Wigner time delay is

$$\tau^i_{\mathrm{W}}(\varepsilon_k, \Omega_{\boldsymbol{k}}) = \frac{\partial}{\partial \varepsilon_k}\mu_i(\varepsilon_k, \Omega_{\boldsymbol{k}}), \text{ where } \mu_i(\varepsilon_k, \Omega_{\boldsymbol{k}}) = \arg\left[a_i(\boldsymbol{k})\right], \quad \text{or} \quad \tau^i_{\mathrm{W}}(\varepsilon_k, \Omega_{\boldsymbol{k}}) = \Im\left[\frac{1}{a_i(\boldsymbol{k})}\frac{\partial a_i(\boldsymbol{k})}{\partial \varepsilon_k}\right]. \tag{3}$$

The analytical expressions for $\partial a(k, \Omega_{\boldsymbol{k}})/\partial\varepsilon_k$ are in appendix D. Evaluating eq. (3) on the energy shell $\varepsilon_k = \varepsilon_{\mathrm{COE}}$ reveals angular modulations with the azimuthal angle of the form $\exp[i(2m_{\mathrm{OAM}} + 2)\varphi]$, while the amplitude of this modulation depends on $\partial\mathcal{E}_+/\partial\varepsilon_k|_{\varepsilon_k=\varepsilon_{\mathrm{COE}}}$. $\partial\mathcal{E}_+/\partial\varepsilon_k|_{\varepsilon_k=\varepsilon_{\mathrm{COE}}}$ depends on the pulse length (number of optical cycles n) and these variations diminish quickly for longer the pulses. The time delay associated with a subshell averaged over m_i is

$$\tau^{n_i\ell_i}_{\mathrm{W}}(\Omega_{\boldsymbol{k}}) = \frac{\sum_{m_i=-\ell_i}^{\ell_i} w_{\ell_i m_i}(\varepsilon_{\mathrm{COE}}, \Omega_{\boldsymbol{k}})\tau^{\ell_i m_i}_{\mathrm{W}}(\varepsilon_{\mathrm{COE}}, \Omega_{\boldsymbol{k}})}{\sum_{m_i=-\ell_i}^{\ell_i} w_{\ell_i m_i}(\varepsilon_{\mathrm{COE}}, \Omega_{\boldsymbol{k}})}. \tag{4}$$

In addition to this quasi analytical model we solved the three-dimensional Schrödinger equation numerically using the matrix iterative method [81, 82]. This numerical algorithm was already tested and implemented in time delay calculations [83, 84] (cf. appendix E for details). The time delays in fig. 2 show, depending on the emission direction, a large difference between the photoionization process from initial states with $m_i = 1$ and $m_i = -1$s. The photoelectron originating from $m_i = 1$ dominates the photoionization probabilities (cf. fig. 1) at the angle $\vartheta_{\boldsymbol{k}} = 90°$, while at $\vartheta_{\boldsymbol{k}} = 150°$ the counter-rotating electron ($m_i = -1$) delivers the largest contribution. The small angular variations in the time delay (in $\varphi_{\boldsymbol{k}}$) smoothen very fast (without affecting the magnitude of the time-delay) for longer pulses (cf. appendix C-E). Experimentally advantageous is the large difference between both cases where the co-rotating or the counter-

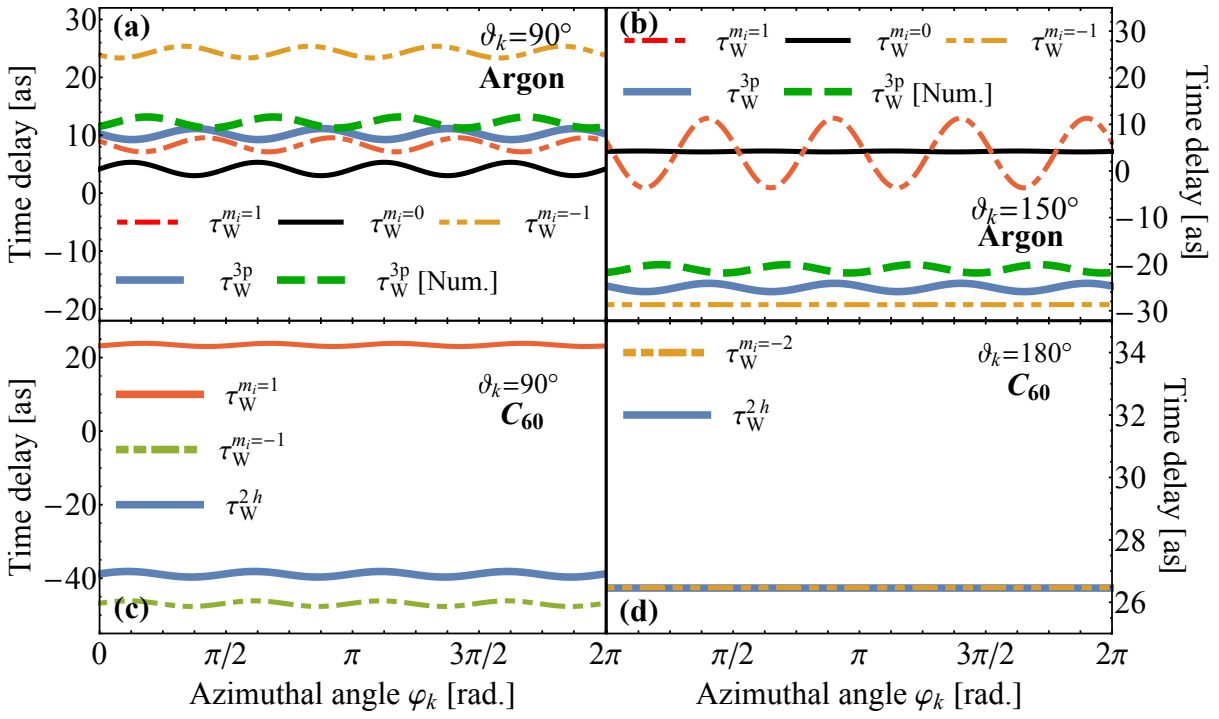

FIG. 2. Time delays for vortex beam ionization of $3p$ subshell of Ar (a and b) as a function of φ_k for different ϑ_k. (c,d) time delay for the vortex pulse ionization of the highest occupied molecular orbitals of C_{60} fullerenes. In (c) $\vartheta_k = 90°$ (electrons with $m_i = -1$ dominate); in (d) $\vartheta_k = 180°$ (mostly electrons from $m_i = -2$ are emitted). Full averaged time delays for the $5h$ subshell are shown.

rotating electrons dominate the photoionization process. The averaged time delay $\tau_W^{3p}(\vartheta_k = 90°) = 10.7$ *as* which coincides almost with the value of $\tau_W^{m_i=1} = 8.7$ *as*. The time delay $\tau_W^{m_i=-1}$ being related to the counter-rotating electron is only a minor contribution to the full subshell delay due to the lower photoionization probability. The electron ionized from the initial state with $m_i = 0$ has no influence on the resulting time delay because we find no photoionization probability in the equatorial plane. The differences between the analytical model and the numerical propagation are vanishingly small giving further credibility to the analytical explanations.

In contrast at $\vartheta_k = 150°$ the fully averaged, subshell time delay $\tau_W^{3p} = -23.5$ *as* is mainly characterized by $\tau_W^{m_i=-1} = -27$ *as*, where the influences of the co-rotating electron ($\tau_W^{m_i=+1} = 3.0$ *as*) and the electron ionized from the initial state with $m_i = 0$ ($\tau_W^{m_i=0} = 4.0$ *as*) play a minor role. Thus, we find a large difference of 34.2 *as* between both cases where either the co-rotating ($m_i = 1$) electron or the counter-rotating electron ($m_i = -1$) dominates. With this configuration it is so possible to pinpoint the origin of the time delay, i.e. a time delay measurement identifies from which initial magnetic sublevel the photoelectron were lauched. From the analytical and symmetry considerations it is conceivable that these findings are of a general nature and are akin to quantized systems with spherical symmetry. This is indeed confirmed by corresponding results (Fig.2c,d) for ionization of C_{60} from the highest occupied molecular levels (HOMO) (see appendix F for full technical details). The 5 electrons in HOMO (or the $5h$ state) occupy the magnetic sublevels $m_i = \pm 2, \pm 1, 0$ which are degenerate but their photoionization probabilities exhibit crossly different angular behavior, as for Ar: In certain directions the photoionization is dominated by emission from specific initial magnetic sublevels of HOMO. As a result, if for instance $\vartheta_k = 90°$ or $\vartheta_k = 180°$ are chosen where photoionization stems largely from $m = -1$ or $m = -2$ respectively, we observe the azimuthal time delay behavior as depicted in Fig. 2c,d. The interpretation goes along the lines as for Ar. The time delays averaged over the initial degeneracies are governed by contributions from the m_i states that dominate the photoionization.

V. SPATIAL DEPENDENCE OF TIME DELAY

Another interesting aspect is the dependence of the time delay in photoionization on the position r_0 of the atom in the OAM XUV laser spot, i.e. away from the optical axis. When the atom is in the donut center the transfer of OAM from the light beam to the photoelectron is maximal, decreasing with enhancing the distance between the atom and optical axis r_0 [56]. This is due to the vast difference in the spatial extension

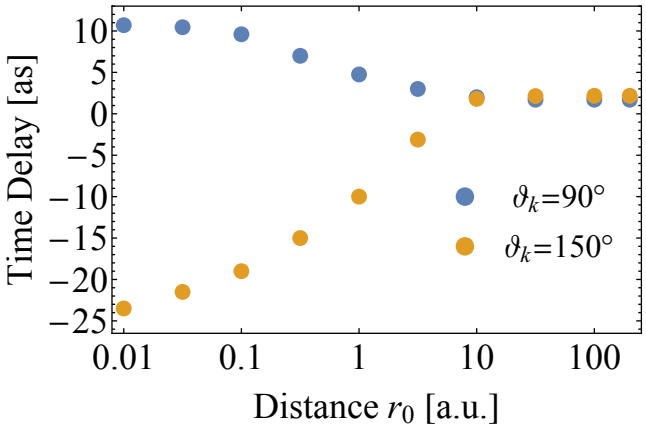

FIG. 3. Time delay variation with the atom distance r_0 from the optical axis. Pulse duration is $n = 10$ optical cycles. Other pulse parameters are as in Fig.(2).

of the atom and the laser spot. Roughly speaking, when the atom is at the peak intensity ($r_0 \approx w_0/\sqrt{2}$) only the beam local spatial structure is relevant, which resembles locally a Gaussian beam [94]. In fig. 3 we show the time delay corresponding to cases where either the co-rotating electron ($\vartheta_k = 90°$) or the counter-rotating electron ($\vartheta_k = 150°$) dominates the photoionization process, as delivered from the full numerical simulations. The numbers at $r_0 = 0$ belong to the results of fig. 2. Surprisingly, even at small distances $r_0 \approx 1$ a.u. the transfer of OAM diminishes rapidly. At distances $r_0 > 10$ a.u. both time delays are nearly indistinguishable. So we argue that measurements of the time delay as a function of the topological charge allows accessing magnetic information with an atomic size spatial resolution using optical beams. This is not a violation of the diffraction limit, as these information are carried by the photoelectron and are not gained via optical microscopy.

VI. CONCLUSIONS

Summarizing, the time delays in photoionization are substantially different for co-rotating (relative to the OAM field) or counter-rotating emitted electrons, even for spherically symmetric targets. The time delay carry atomic-scale information on the orbital position in the beam spot. Including spin-orbital coupling, e.g., as done in [85] should yield spin-dependent time delays offering a tool for polarized electron burst [86] by short OAM pulses. Combined with the possible spatial resolution on the magnetic states, this may offer a novel technique for spatio-temporal mapping of spin dynamics.

ACKNOWLEDGMENTS

The work is supported by the DFG through SPP 1840. We thank Olga Smirnova and Ingo Barth for interesting discussions.

Appendix A: Modelling propagating OAM beams

The OAM beam vector potential in the coordinate frame of the atom with the z axis being parallel to the light propagation (with a wave vector q_z) is [87]

$$\boldsymbol{A}(\boldsymbol{r},t) = \hat{\epsilon} A_0 f^p_{m_{\rm OAM}}(\boldsymbol{r}) e^{i\left[m_{\rm OAM}\varphi'(\boldsymbol{r})-\omega t\right]} g(t) e^{iq_z z'(\boldsymbol{r})} + \text{c.c.}. \quad \text{(A1)}$$

The polarization vector is taken $\hat{\epsilon} = (1, i)^T$, and for the pulse temporal envelope we take

$$g(t) = \cos[\pi t/nT]^2,$$

where $T = 2\pi/\omega$ is the cycle duration and n is the number of optical cycles. $\varphi'(\boldsymbol{r})$ is the electron azimuthal angle relative to the optical axis of the laser field. If the atom is in the beam center we write $\varphi'(\boldsymbol{r}) \equiv \varphi$. For the photon energies of concern here $q_z z'(\boldsymbol{r}) \ll 1$ applies, i.e. the dipole approximation is acceptable along the z axis. The radial structure is described by the function

$$f^p_{m_{\rm OAM}}(\boldsymbol{r}) = e^{-\frac{\rho'(\boldsymbol{r})^2}{w_0^2}} \left(\frac{\sqrt{2}\rho'(\boldsymbol{r})}{w_0}\right)^{|m_{\rm OAM}|} L_p^{|m_{\rm OAM}|}\left(\frac{2\rho'(\boldsymbol{r})^2}{w_0^2}\right), \quad \text{(A2)}$$

where $\rho'(\boldsymbol{r})$ is the radial distance to the optical axis. If the atom is in the beam center then $\rho'(\boldsymbol{r}) = r\sin\vartheta$. The number of nodes in the beam radial profile is indexed by p and $L_p^{|m_{\rm OAM}|}(x)$ are the generalized Laguerre polynomials. We consider the experimentally important case $p = 0$ for which $L_p^{|m_{\rm OAM}|}(x) = 1$. Calculations for $p \neq 0$ are feasible but are not expected to yield any sizable effect on the time delay (the beam radial variation is on the scale of tens of nanometers, i.e. far off the electron wavelength). w_0 stands for the beam waist. Typical values that we employed in the calculations are in the range of $w_0 = 50$ nm (940 a.u.). Obviously $|\mathbf{A}|^2$ possess a donut shape for $p = 0$ and intercalated rings for $p > 1$.

Appendix B: Transition amplitude

For the analytical model and the situation detailed in the main text the optical-vertex matrix elements between the initial and final states are (we exploited $\boldsymbol{p} = -\left[\hat{H}_0, \boldsymbol{r}\right]_-$) $\langle\varphi_{\boldsymbol{k}}^{(-)}|\hat{H}_{int}(t)|\Psi_i\rangle = i(\varepsilon_i - \varepsilon_{\boldsymbol{k}})\langle\varphi_{\boldsymbol{k}}^{(-)}|\boldsymbol{r}\cdot\boldsymbol{A}(\boldsymbol{r},t)|\Psi_i\rangle$. After the laser

pulse is off we infer

$$a_i(\boldsymbol{k}) = (\varepsilon_i - \varepsilon_{\boldsymbol{k}}) \sum_{\ell=0} \sum_{m=-\ell}^{m=\ell} i^{-\ell} e^{i\delta_\ell(k)} d^{m_{\rm OAM}}_{\ell,n_i\ell_i} Y_{\ell m}(\Omega_{\boldsymbol{k}}) \times \left[\mathcal{E}_-(\varepsilon_{\boldsymbol{k}} - \varepsilon_i) \begin{pmatrix} \ell & m_{\rm OAM}+1 & \ell_i \\ -m & m_{\rm OAM}+1 & m_i \end{pmatrix} + \mathcal{E}_+(\varepsilon_{\boldsymbol{k}} - \varepsilon_i) \begin{pmatrix} \ell & m_{\rm OAM}+1 & \ell_i \\ -m & -m_{\rm OAM}-1 & m_i \end{pmatrix} \right], \tag{B1}$$

where $\mathcal{E}_\mp(\varepsilon) = \mathcal{E}_0 \int_{-\infty}^{\infty} \mathrm{d}t\, g(t) e^{i(\varepsilon \mp \omega)t}$ and $\mathcal{E}_0 = A_0 \left(\frac{\sqrt{2}}{w_0}\right)^{|m_{\rm OAM}|}$. The reduced radial matrix elements are given by

$$d^{m_{\rm OAM}}_{\ell,n_i\ell_i} = \sqrt{\frac{(2\ell+1)(2m_{\rm OAM}+3)(2\ell_i+1)}{3}} \times \begin{pmatrix} \ell & m_{\rm OAM}+1 & \ell_i \\ 0 & 0 & 0 \end{pmatrix} \int \mathrm{d}r\, r^{3+m_{\rm OAM}} R_{k\ell}(r) R_i(r). \tag{B2}$$

Appendix C: Details to the numerical propagation scheme

Numerically, we follow a standard matrix iterative method: The time dependent wave function is expanded in spherical harmonics, i.e. $\Psi(\boldsymbol{r},t) = \sum_{\ell=0}^{L_{\rm max}} \sum_{m=-\ell}^{\ell} R_\ell(r) Y_{\ell m}(\Omega_{\boldsymbol{r}})$ with $\lim_{t\to-\infty} \Psi(\boldsymbol{r},t) = \Psi_i(\boldsymbol{r},t)$. Every initial state of Ar 3p subshell is propagated from $t = -0.5T$ to $0.5T$ in the presence of the OAM laser field. At a time where the photoelectron wave packet is fully formed, the solution $\Psi(\boldsymbol{r}, t > 0.5T)$ is then projected onto a set of field-free scattering wave function $\varphi^{(-)}_{\boldsymbol{k}}(\boldsymbol{r})$ and we obtain the photoionization amplitudes $a_i(\boldsymbol{k})$ associated with the specific initial state i, which are further analyzed to extract the time delay.

Appendix D: Time Delay

The Wigner time delay in photoionization is given by

$$\tau^i_{\rm W}(\varepsilon_k, \Omega_{\boldsymbol{k}}) = \frac{\partial}{\partial \varepsilon_k} \mu_i(\varepsilon_k, \Omega_{\boldsymbol{k}}), \tag{D1}$$

where $\mu_i(\varepsilon_k, \Omega_{\boldsymbol{k}}) = \arg[a_i(\boldsymbol{k})]$ or by

$$\tau^i_{\rm W}(\varepsilon_k, \Omega_{\boldsymbol{k}}) = \Im \left[\frac{1}{a_i(\boldsymbol{k})} \frac{\partial a_i(\boldsymbol{k})}{\partial \varepsilon_k} \right]. \tag{D2}$$

Taking into account that $\partial\mathcal{E}_-/\partial\varepsilon_k = 0$ (absorption) while $\partial\mathcal{E}_+/\partial\varepsilon_k \neq 0$ (emission) at $\varepsilon_k = \varepsilon_{\rm COE}$, we find the following expression for the energy derivative of the amplitude in case of $m_i = 1$

$$\left.\frac{\partial a(k,\Omega_{\boldsymbol{k}})}{\partial \varepsilon_k}\right|_{\varepsilon_k=\varepsilon_{\rm COE}} = \frac{\partial S_{m_{\rm OAM}+2, m_{\rm OAM}+2}}{\partial \varepsilon_k} Y_{m_{\rm OAM}+2, m_{\rm OAM}+2}(\Omega_{\boldsymbol{k}}) + F_{m_{\rm OAM}, -m_{\rm OAM}} Y_{m_{\rm OAM}, -m_{\rm OAM}}(\Omega_{\boldsymbol{k}}) + F_{m_{\rm OAM}+2, -m_{\rm OAM}} Y_{m_{\rm OAM}+2, -m_{\rm OAM}}(\Omega_{\boldsymbol{k}}) \tag{D3}$$

where

$$F_{\ell,m} = \left.\frac{\partial \mathcal{E}_+}{\partial \varepsilon_k} d^{m_{\rm OAM}}_{\ell,n_i\ell_i} i^{-\ell}(k) e^{i\delta_\ell(k)} \begin{pmatrix} \ell & m_{\rm OAM}+1 & 1 \\ -m & -m_{\rm OAM}-1 & m_i \end{pmatrix}\right|_{\varepsilon_k=\varepsilon_{\rm COE}} \tag{D4}$$

incorporates the emission coefficient. Along the same lines we obtain for $m_i = 0$

$$\left.\frac{\partial a(k,\Omega_{\boldsymbol{k}})}{\partial \varepsilon_k}\right|_{\varepsilon_k=\varepsilon_{\rm COE}} = \frac{\partial S_{m_{\rm OAM}+2, m_{\rm OAM}+1}}{\partial \varepsilon_k} Y_{m_{\rm OAM}+2, m_{\rm OAM}+1}(\Omega_{\boldsymbol{k}}) + F_{m_{\rm OAM}+2, -m_{\rm OAM}-1} Y_{m_{\rm OAM}+2, -m_{\rm OAM}-1}(\Omega_{\boldsymbol{k}}) \tag{D5}$$

and for $m_i = -1$

$$\left.\frac{\partial a(k,\Omega_{\boldsymbol{k}})}{\partial \varepsilon_k}\right|_{\varepsilon_k=\varepsilon_{\rm COE}} = \frac{\partial S_{m_{\rm OAM}+2, m_{\rm OAM}}}{\partial \varepsilon_k} Y_{m_{\rm OAM}+2, m_{\rm OAM}}(\Omega_{\boldsymbol{k}}) + \frac{\partial S_{m_{\rm OAM}, m_{\rm OAM}}}{\partial \varepsilon_k} Y_{m_{\rm OAM}, m_{\rm OAM}}(\Omega_{\boldsymbol{k}}) + F_{m_{\rm OAM}+2, -m_{\rm OAM}-2} Y_{m_{\rm OAM}+2, -m_{\rm OAM}-2}(\Omega_{\boldsymbol{k}}). \tag{D6}$$

Appendix E: Analytical vs. numerical results

To facilitate the comparison between the analytical and the numerical results for the delay time as the pulse duration varies we refer to Fig. 4 of this supplementary materials that should be compared with Fig.2 of the main text. It is obvious that for longer pulse durations (meaning more optical cycles n) the small variations in the dependence on the azimuthal angle $\varphi_{\boldsymbol{k}}$ diminish.

Appendix F: Time delay in photoionization of C_{60} molecule

Due to the vast difference between the atomic orbital extent and the focused, but diffraction limited laser spot the predicted effects for atoms require highly intense laser pulses. For instance, the Ar calculations in the main text were performed for a peak intensity of 5.6×10^{19} W/cm^2 at $w_0/\sqrt{2}$. For more extended orbitals similar effects in photoionization are achieved at lower peak intensity which is advantageous from an experimental point of view. To endorse and quantify this statement we considered C_{60} as the next step from atoms towards extended systems. The radius of the carbon cage of C_{60} is $R_{C_{60}} = 6.745\,a_B$. Assuming an $A_0 = 0.05$ a.u. at $R_{C_{60}}$ we find a peak intensity of 3.2×10^{17} W/cm^2 at $w_0/\sqrt{2}$. In principle, one may consider C_{240} to lower the peak intensity even more.

To apply our theory we describe the molecule with an effective single particle potential that captures the valence electronic structure with its characteristics as derived accounting for the I_h-symmetry. Technically, as an input we use the correlated, ab-initio calculated, single particle density $n(r)$ which incorporates the underlying ionic structure to construct a local single particle (orbital-dependent) potential [88–90]. This

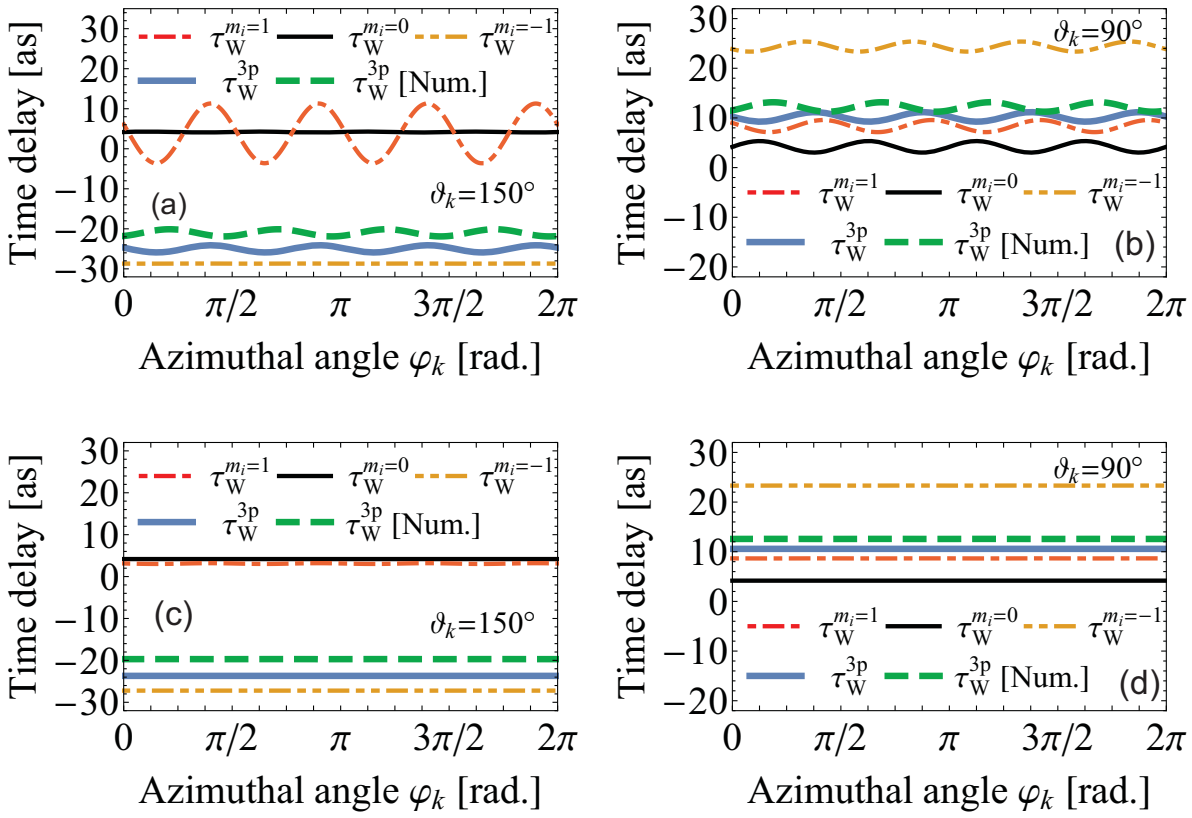

FIG. 4. Dependence of the time delays on the pulse duration. This figure is to be compared with Fig.2 of the main text. For the upper panels the pulse consists of $n = 3$ optical cycles, while for the lower panels the pulse has $n = 10$. Other pulse parameters are the same as in Fig.2 of the main text. For $\vartheta_k = 150°$ the averaged time delay stems from states with $m_i = -1$, whereas for $\vartheta_k = 90°$ states with $m_i = +1$ deliver the major contribution to the averaged time delay (note, the ionization probability for $m_i = -1$ in this region is suppressed).

potential is utilized for the driven electron dynamics [89, 91]. Using the constructed potential, the electronic wave function $\Psi(r)$ of the fullerene valence shell is expressible as a product of a radial part $R_{n_i}(r)$ with $n_i - 1$ nodes, and an angular part characterized by the spherical harmonics $Y_{\ell_i m_i}(\Omega_r)$ with the orbital and magnetic quantum numbers ℓ_i and m_i. The corresponding energies (degenerate in m_i) are $\varepsilon_{n_i\ell_i}$. Within this model the occupied valence states form two radial (σ and π) subbands. The wave functions are shown in fig. 5. The occupation of the single-particle orbitals were discussed in Ref. [92] with the HOMO orbital ($n_i = 2, \ell_i = 5$) being occupied by 5 electrons. C_{60} has a diamagnetic character with the HOMO magnetic sublevels $m_i = -2, -1, 0, 1, 2$ being populated.

In fig. 6(a) we present the radial matrix elements which are relevant for the photoionization process of the HOMO orbital. For the same reason as in the main text we choose a frequency regime where the matrix elements have similar magnitudes (in which case $\hbar\omega_{\mathrm{XUV}} = 60\,\mathrm{eV}$). In panel fig. 6(b) we show the corresponding photoionization probabilities $\left|a_{\ell_i=5,m_i}(k_{\mathrm{COE}}, \vartheta_{\boldsymbol{k}})\right|^2$ of the different initial states from the $5h$ orbital in C_{60} in dependence on the polar angle $\vartheta_{\boldsymbol{k}}$ relative to the optical axis of the vortex field. The figure demonstrates the significantly different angular distributions for photoelectrons originating from different initial states which endorses the generality of the predicted effect. Clearly, one may follow the arguments made for Ar in the main text and reach the same conclusions for C_{60}: We find directions where the photoionization process is totally dominated by some specific initial magnetic sublevel of the HOMO. This has also a direct consequence for the time delay depicted in panel fig. 6(c) and (d).

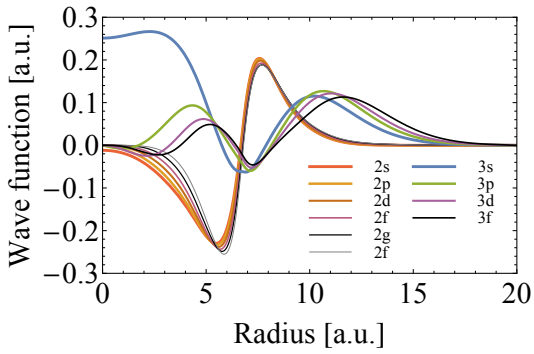

FIG. 5. The real radial wave functions of the electronic states for different orbital quantum numbers.

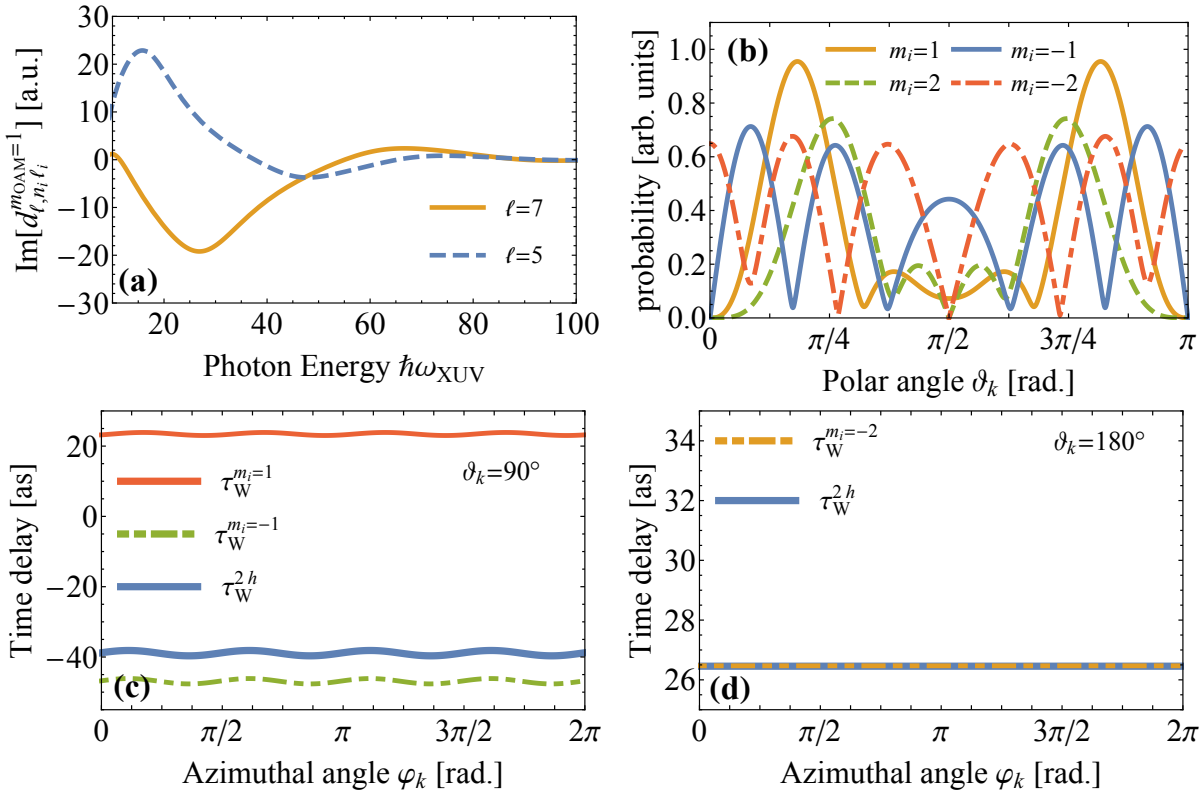

FIG. 6. (a) Reduced radial matrix elements for the partial wave functions with the orbital angular momenta $\ell = 5$ and $\ell = 7$. (b) Angular dependent photoionization probabilities for the different initial states of the $5h$ subshell (HOMO) in C_{60}. (c)-(d) The time delays vary with the azimuthal angle φ_k at the polar angle ϑ_k. The left column corresponds to the photoionization process for $\vartheta_k = 90°$ (electrons with $m_i = -1$ are dominant), while the right column is associated with $\vartheta_k = 180°$ (electrons with $m_i = -2$ are dominant). Time delays for the $5h$ subshell averaged over the initial states degeneracies are also shown.

We choose here as examples the polar angles $\vartheta_k = 90°$ and $\vartheta_k = 180°$, where according to the photoionization probabilities are dominated by emission from respectively the $m_i = -1$ and $m_i = -2$ states. The duration of the pulse is $n = 3$ optical cycles. The small variations as the azimuthal angle φ_k varies decrease for longer pulses. We show only time delays of electrons which have a photoionization probability $\left|a_{\ell=5,m}(k_{\rm COE}, \vartheta_k)\right|^2 > 0$. The time delay averaged over initial state degeneracies receives major contributions from specific magnetic sublevels at certain directions as in the case of Argon atom.

[1] Attosecond photonics (focus issue) *Nat. Photon.* **8**, 161-264 (2014).
[2] R. Pazourek, S. Nagele, J. Burgdörfer, Attosecond chronoscopy of photoemission. *Rev. Mod. Phys.* **87**, 765 (2015).
[3] L. Torlina, *et al.*, Interpreting attoclock measurements of tunnelling times. *Nat. Phys.* **11**, 503–508 (2015).
[4] A. Maquet, J. Caillat, R. Taïeb, Attosecond delays in photoionization: Time and quantum mechanics. *J. Phys. B: At. Mol. Opt. Phys.* **47**, 204004 (2014).
[5] J. Dahlström, A. LHuillier, A. Maquet, Introduction to attosecond delays in photoionization. *J. Phys. B: At. Mol. Opt. Phys.* **45**, 183001 (2012).
[6] A. S. Landsman, U. Keller, Attosecond science and the tunnelling time problem. *Phys. Rep.* **547**, 1–24 (2015).
[7] J. Su, H. Ni, A. Becker, A. Jaroń-Becker, Numerical simulation of time delays in light-induced ionization. *Phys. Rev. A* **87**, 033420 (2013).
[8] L. E. Eisenbud, *PhD thesis* (Princeton University, 1948).
[9] E. P. Wigner, Lower limit for the energy derivative of the scattering phase shift. *Phys. Rev.* **98**, 145–147 (1955).
[10] C. Joachain, *Quantum collision theory* (North-Holland, Amsterdam, 1975).
[11] M. Schultze, *et al.*, Delay in photoemission. *Science* **328**, 1658-1662 (2010).
[12] K. Klünder, *et al.*, Probing single-photon ionization on the attosecond time scale. *Phys. Rev. Lett.* **106**, 143002 (2011).
[13] D. Guénot, *et al.*, Photoemission-time-delay measurements and calculations close to the 3 s-ionization-cross-section minimum in ar. *Phys. Rev. A* **85**, 053424 (2012).

[14] A. Kheifets, I. Ivanov, Delay in atomic photoionization. *Physical review letters* **105**, 233002 (2010).

[15] S. Nagele, *et al.*, Time-resolved photoemission by attosecond streaking: extraction of time information. *J. Phys. B: At. Mol. Opt. Phys.* **44**, 081001 (2011).

[16] C.-H. Zhang, U. Thumm, Streaking and wigner time delays in photoemission from atoms and surfaces. *Phys. Rev. A* **84**, 033401 (2011).

[17] L. Moore, M. Lysaght, J. Parker, H. van der Hart, K. Taylor, Time delay between photoemission from the 2 p and 2 s subshells of neon. *Phys. Rev. A* **84**, 061404 (2011).

[18] S. Nagele, R. Pazourek, J. Feist, J. Burgdörfer, Time shifts in photoemission from a fully correlated two-electron model system. *Phys. Rev. A* **85**, 033401 (2012).

[19] J. Dahlström, T. Carette, E. Lindroth, Diagrammatic approach to attosecond delays in photoionization. *Phys. Rev. A* **86**, 061402 (2012).

[20] J. M. Dahlström, *et al.*, Theory of attosecond delays in laser-assisted photoionization. *Chem. Phys.* **414**, 53–64 (2013).

[21] A. Kheifets, Time delay in valence-shell photoionization of noble-gas atoms. *Phys. Rev. A* **87**, 063404 (2013).

[22] G. Dixit, H. S. Chakraborty, M. E.-A. Madjet, Time delay in the recoiling valence photoemission of ar endohedrally confined in c 60. *Phys. Rev. Lett.* **111**, 203003 (2013).

[23] J. Feist, *et al.*, Time delays for attosecond streaking in photoionization of neon. *Phys. Rev. A* **89**, 033417 (2014).

[24] J. M. Dahlström, E. Lindroth, Study of attosecond delays using perturbation diagrams and exterior complex scaling. *J. Phys. B: At. Mol. Opt. Phys.* **47**, 124012 (2014).

[25] J. Wätzel, A. Moskalenko, Y. Pavlyukh, J. Berakdar, Angular resolved time delay in photoemission. *J. Phys. B: At. Mol. Opt. Phys.* **48**, 025602 (2015).

[26] L. Allen, M. W. Beijersbergen, R. J. C. Spreeuw, J. P. Woerdman, Orbital angular momentum of light and the transformation of laguerre-gaussian laser modes. *Phys. Rev. A* **45**, 8185–8189 (1992).

[27] M. Beijersbergen, L. Allen, H. van der Veen, J. Woerdman, Astigmatic laser mode converters and transfer of orbital angular momentum. *Opt. Commun.* **96**, 123 - 132 (1993).

[28] M. Beijersbergen, R. Coerwinkel, M. Kristensen, J. Woerdman, Helical-wavefront laser beams produced with a spiral phaseplate. *Opt. Commun.* **112**, 321–327 (1994).

[29] H. He, M. Friese, N. Heckenberg, H. Rubinsztein-Dunlop, Direct observation of transfer of angular momentum to absorptive particles from a laser beam with a phase singularity. *Phys. Rev. Lett.* **75**, 826 (1995).

[30] N. Simpson, K. Dholakia, L. Allen, M. Padgett, Mechanical equivalence of spin and orbital angular momentum of light: an optical spanner. *Opt. Lett.* **22**, 52–54 (1997).

[31] M. Soskin, V. Gorshkov, M. Vasnetsov, J. Malos, N. Heckenberg, Topological charge and angular momentum of light beams carrying optical vortices. *Phys. Rev. A* **56**, 4064 (1997).

[32] L. Allen, S. M. Barnett, M. Padgett, *Optical Angular Momentum* (Institute of Physics Publishing, Bristol, 2003).

[33] O. S. Magana-Loaiza, M. Mirhosseini, R. M. Cross, S. M. H. Rafsanjani, R. W. Boyd, Hanbury Brown and Twiss interferometry with twisted light. *Sci. Adv.* **2**, e1501143 (2016).

[34] M. E. J. Friese, T. A. Nieminen, N. R. Heckenberg, H. Rubinsztein-Dunlop, Optical alignment and spinning of laser-trapped microscopic particles. *Nature* **394**, 348 (1998).

[35] A. T. O'Neil, I. MacVicar, L. Allen, M. J. Padgett, Intrinsic and extrinsic nature of the orbital angular momentum of a light beam. *Phys. Rev. Lett.* **88**, 053601 (2002).

[36] N. B. Simpson, K. Dholakia, L. Allen, M. J. Padgett, Mechanical equivalence of spin and orbital angular momentum of light: an optical spanner. *Opt. Lett.* **22**, 52–54 (1997).

[37] K. T. Gahagan, G. A. Swartzlander, Optical vortex trapping of particles. *Opt. Lett.* **21**, 827–829 (1996).

[38] M. Babiker, W. Power, L. Allen, Light-induced torque on moving atoms. *Phy. Rev. Lett.* **73**, 1239 (1994).

[39] D. L. Andrews, M. Babiker, *The angular momentum of light* (Cambridge University Press, 2012).

[40] J. Wätzel, A. S. Moskalenko, J. Berakdar, Photovoltaic effect of light carrying orbital angular momentum on a semiconducting stripe. *Opt. Expr.* **20**, 27792-27799 (2012).

[41] G. Molina-Terriza, J. P. Torres, L. Torner, Twisted photons. *Nat. Phys.* **3**, 305-310 (2007).

[42] A. Mair, A. Vaziri, G. Weihs, A. Zeilinger, Entanglement of the orbital angular momentum states of photons. *Nature* **412**, 313–316 (2001).

[43] J. T. Barreiro, T.-C. Wei, P. G. Kwiat, Beating the channel capacity limit for linear photonic superdense coding. *Nat. Phys.* **4**, 282–286 (2008).

[44] R. W. Boyd, *et al.*, *SPIE OPTO* (International Society for Optics and Photonics, 2011), pp. 79480L–79480L.

[45] M. Padgett, R. Bowman, Tweezers with a twist. *Nat. Phot.* **5**, 343–348 (2011).

[46] S. Fürhapter, A. Jesacher, S. Bernet, M. Ritsch-Marte, Spiral interferometry. *Opt. Lett.* **30**, 1953–1955 (2005).

[47] M. Woerdemann, C. Alpmann, C. Denz, Self-pumped phase conjugation of light beams carrying orbital angular momentum. *Opt. Expr.* **17**, 22791–22799 (2009).

[48] J. P. Torres, L. Torner, *Twisted Photons: Applications of Light with Orbital Angular Momentum* (Wiley-VCH, Weinsheim, 2011).

[49] D. L. Andrews, *Structured light and its applications: An introduction to phase-structured beams and nanoscale optical forces* (Academic Press, 2011).

[50] G. Foo, D. M. Palacios, G. A. Swartzlander Jr, *et al.*, Optical vortex coronagraph. *Opt. Lett.* **30**, 3308–3310 (2005).

[51] H. He, N. Heckenberg, H. Rubinsztein-Dunlop, Optical particle trapping with higher-order doughnut beams produced using high efficiency computer generated holograms. *J. Mod. Opt.* **42**, 217–223 (1995).

[52] H. Wang, L. Shi, B. Lukyanchuk, C. Sheppard, C. T. Chong, Creation of a needle of longitudinally polarized light in vacuum using binary optics. *Nat. Phot.* **2**, 501–505 (2008).

[53] S. W. Hell, Far-field optical nanoscopy. *Science* **316**, 1153–1158 (2007).

[54] A. Picón, *et al.*, Photoionization with orbital angular momentum beams. *Opt. Expr.* **18**, 3660–3671 (2010).

[55] K. Köksal, J. Berakdar, Charge-current generation in atomic systems induced by optical vortices. *Phys. Rev. A* **86**, 063812 (2012).

[56] J. Wätzel, Y. Pavlyukh, A. Schäaffer, J. Berakdar, Optical vortex driven charge current loop and optomagnetism in fullerenes. *Carbon* **99**, 439 - 443 (2016).

[57] R. Géneaux, *et al.*, Attosecond light and electronic vortices. *arXiv preprint arXiv:1509.07396* (2015).

[58] G. Gariepy, *et al.*, Creating high-harmonic beams with controlled orbital angular momentum. *Phys. Rev. Lett.* **113**, 153901 (2014).

[59] M. Zürch, C. Kern, P. Hansinger, A. Dreischuh, C. Spielmann, Strong-field physics with singular light beams. *Nat. Phys.* **8**, 743–746 (2012).

[60] J. Vieira, *et al.*, Amplification and generation of ultra-intense twisted laser pulses via stimulated raman scattering. *Nat.*

Comm. **7** (2016).
[61] X. Zhang, *et al.*, Generation of intense high-order vortex harmonics. *Phys. Rev. Lett.* **114**, 173901 (2015).
[62] A. Ashkin, J. Dziedzic, J. Bjorkholm, S. Chu, Observation of a single-beam gradient force optical trap for dielectric particles. *Opt. Lett.* **11**, 288–290 (1986).
[63] D. Meschede, Optics, light and lasers: the practical approach to modern aspects of photonics and laser physics, optik, licht und laser engl (2007).
[64] O. Matula, A. G. Hayrapetyan, V. G. Serbo, A. Surzhykov, S. Fritzsche, Atomic ionization of hydrogen-like ions by twisted photons: angular distribution of emitted electrons. *J. Phys. B: At. Mol. Opt. Phys.* **46**, 205002 (2013).
[65] A. Afanasev, C. E. Carlson, A. Mukherjee, Off-axis excitation of hydrogenlike atoms by twisted photons. *Phys. Rev. A* **88**, 033841 (2013).
[66] A. Picón, *et al.*, Transferring orbital and spin angular momenta of light to atoms. *New J. Phys.* **12**, 083053 (2010).
[67] R. Pazourek, S. Nagele, J. Burgdörfer, Time-resolved photoemission on the attosecond scale: opportunities and challenges. *Faraday discussions* **163**, 353–376 (2013).
[68] S. Heuser, *et al.*, *J. Phys. Conf. Ser.* (2015), vol. 635, p. 092089.
[69] C. Hernández-García, A. Picón, J. San Román, L. Plaja, Attosecond extreme ultraviolet vortices from high-order harmonic generation. *Phys. Rev. Lett.* **111**, 083602 (2013).
[70] C. Hernandez-Garcia, A. Picon, J. San Roman, L. Plaja, *Laser Science* (Optical Society of America, 2014), pp. LW5H–6.
[71] X. Zhang, *et al.*, Generation of intense high-order vortex harmonics. *Phys. Rev. Lett* **114**, 173901 (2015).
[72] H. Muller, Numerical simulation of high-order above-threshold-ionization enhancement in argon. *Phys. Rev. A* **60**, 1341 (1999).
[73] E. Toma, H. Muller, Calculation of matrix elements for mixed extreme-ultraviolet–infrared two-photon above-threshold ionization of argon. *J. Phys. B: At. Mol. Opt. Phys.* **35**, 3435 (2002).
[74] J. Higuet, *et al.*, High-order harmonic spectroscopy of the cooper minimum in argon: Experimental and theoretical study. *Phys. Rev. A* **83**, 053401 (2011).
[75] I. Barth, O. Smirnova, Hole dynamics and spin currents after ionization in strong circularly polarized laser fields. *J. Phys. B: At. Mol. Opt. Phys.* **47**, 204020 (2014).
[76] I. Barth, O. Smirnova, Spin-polarized electrons produced by strong-field ionization. *Phys. Rev. A* **88**, 013401 (2013).
[77] M. V. Fedorov, *Atomic and free electrons in a strong light field*, vol. 452 (World Scientific, 1997).
[78] M. Y. Amusia, *Atomic photoeffect* (Springer Science & Business Media, 2013).
[79] M. Y. Amusia, L. V. Chernysheva, *Computation of atomic processes: A handbook for the ATOM programs* (Institute of physics, 1997).
[80] J. W. Cooper, Photoionization from outer atomic subshells. a model study. *Phys. Rev.* **128**, 681 (1962).
[81] M. Nurhuda, F. H. Faisal, Numerical solution of time-dependent schrödinger equation for multiphoton processes: A matrix iterative method. *Phys. Rev. A* **60**, 3125 (1999).
[82] A. N. Grum-Grzhimailo, B. Abeln, K. Bartschat, D. Weflen, T. Urness, Ionization of atomic hydrogen in strong infrared laser fields. *Phys. Rev. A* **81**, 043408 (2010).
[83] I. Ivanov, Time delay in strong-field photoionization of a hydrogen atom. *Phys. Rev. A* **83**, 023421 (2011).
[84] I. Ivanov, A. Kheifets, Time delay in atomic photoionization with circularly polarized light. *Phys. Rev. A* **87**, 033407 (2013).
[85] G. Quinteiro, P. Tamborenea, J. Berakdar, Orbital and spin dynamics of intraband electrons in quantum rings driven by twisted light. *Opt. Expr.* **19**, 26733–26741 (2011).
[86] N. Clayburn, *et al.*, Search for spin-polarized photoemission from gas using light with orbital angular momentum. *Phys. Rev. B* **87**, 035204 (2013).
[87] L. Allen, M. W. Beijersbergen, R. Spreeuw, J. Woerdman, *Phys. Rev. A* **45**, 8185 (1992).
[88] Y. Pavlyukh and J. Berakdar, Chem. Phys. Lett. **468**, 313 (2009).
[89] Y. Pavlyukh and J. Berakdar, J. Chem. Phys. **135**, 201103 (2011).
[90] Y. Pavlyukh and J. Berakdar, Phys. Rev. A **81**, 042515 (2010).
[91] A. Moskalenko, Y. Pavlyukh, and J. Berakdar, Phys. Rev. A **86**, 013202 (2012).
[92] R. Haddon, L. E. Brus, and K. Raghavachari, Chem. Phys. Lett. **125**, 459 (1986) .
[93] The conventional time delay angular modulation is substantial for atomic systems with a Cooper minimum, otherwise it is quite small [25]. Recently, it was measured for Helium [68] and been traced back to interplay between two final quantum states accessible by two photons.
[94] This amounts to an intensity at $w_0/\sqrt{2}$ of 5.6×10^{19} W/cm^{-2}.
[95] Analyzing optical transitions for $r_0 \approx w_0/\sqrt{2}$ leads to dipole selection rules $\ell_i \to \ell_i+1$ ($\ell_i \to \ell_i-1$) and $m_i \to m_i+1$. This is because the angular momentum associated with the photon spin has no spatial dependence and for larger $r_0 > 10$ a.u. the whole process resembles photoionization with conventional circularly polarized light [84].